Journal of Solid State Chemistry 184 (2011) 1165–1171

Contents lists available at ScienceDirect

Journal of Solid State Chemistry

journal homepage: www.elsevier.com/locate/jssc

Morphology-controlled synthesis and novel microwave electromagnetic properties of hollow urchin-like chain Fe-doped MnO_2 under 10 T high magnetic field

Duan Yuping*, Zhang Jia, Jing Hui, Liu Shunhua

Department of Materials Processing Engineering, School of Materials Science & Engineering, Dalian University of Technology, Linggong Road 2, Ganjingzi District, Dalian, Liaoning Province 116085, PR China

ARTICLE INFO

Article history:
Received 25 September 2010
Received in revised form
27 January 2011
Accepted 3 March 2011
Available online 21 March 2011

Keywords:
Fe-doped MnO_2
High magnetic field
Electromagnetic properties

ABSTRACT

Fe-doped MnO_2 with a hollow sea urchin-like ball chain shape was first synthesized under a high magnetic field of 10 T. The formation mechanism was investigated and discussed in detail. The synthesized samples were characterized by XRD, SEM, TEM, EMPA, and vector network analysis. By doping MnO_2 with Fe, the relative complex permittivity of MnO_2 and its corresponding loss tangent clearly decreases, but its relative complex permeability and its corresponding loss tangent markedly increases. Moreover, the theoretically calculated values of reflection loss show that with increasing the Fe content, the as-prepared Fe-doped MnO_2 exhibits good microwave absorption capability.

1. Introduction

In recent years, electromagnetic (EM) pollution has worsened and has become another serious environmental problem, after air and water pollution. In light of this, EM wave absorbents have attracted considerable interest because of the increasing civil, commercial, and military applications presented by EM wave shielding and absorbance in the gigahertz (GHz) band range [1]. EM wave absorbents are desired because these possess both excellent dielectric loss and magnetic loss properties.

The outstanding structural flexibility of MnO_2 and its derivative compounds, in combination with their novel chemical and physical properties, has paved the way for their wide use as catalysts [2], molecular sieves [3], components in Li/MnO_2 batteries [4], and EM wave absorbents [5]. MnO_2 as an EM wave absorbent has good dielectric loss properties, but its magnetic loss properties are relatively poor [6]. Given that MnO_2 properties are strongly dependent on parameters such as powder morphology, crystallinity structure, or bulk density, several groups have synthesized MnO_2 powder using an in situ redox process and doping a metallic element or an organic template into the compound to improve its morphology and properties. Tang et al. [7,8] studied the synthesis and magnetic properties of MnO_2 nanorods and layered MnO_2 nanowire bundles. Patrice et al. [9] synthesized Fe-substituted MnO_2 samples to improve the electrochemical properties of MnO_2. Liu et al. [10] prepared hierarchically structured mesoporous MnO_2 and Mn_2O_3 using L-lysine as a template. Li et al. [11] synthesized orchid-like Cr-doped MnO_2 nanostructures. In these studies, the morphology

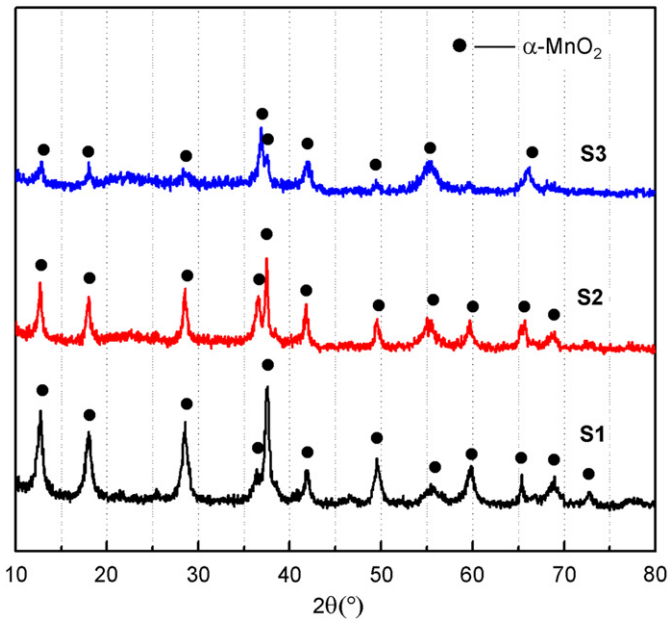

Fig. 1. X-ray diffraction patterns of S1, S2 and S3. S1: sample without Fe; S2: with an Fe/Mn proportions of 1/9; S3: with an Fe/Mn proportion of 1/4.

* Corresponding author. Fax: +86 411 84708446.
E-mail address: duanyp@dlut.edu.cn (D. Yuping).

0022-4596/$ - see front matter © 2011 Elsevier Inc. All rights reserved.
doi:10.1016/j.jssc.2011.03.007

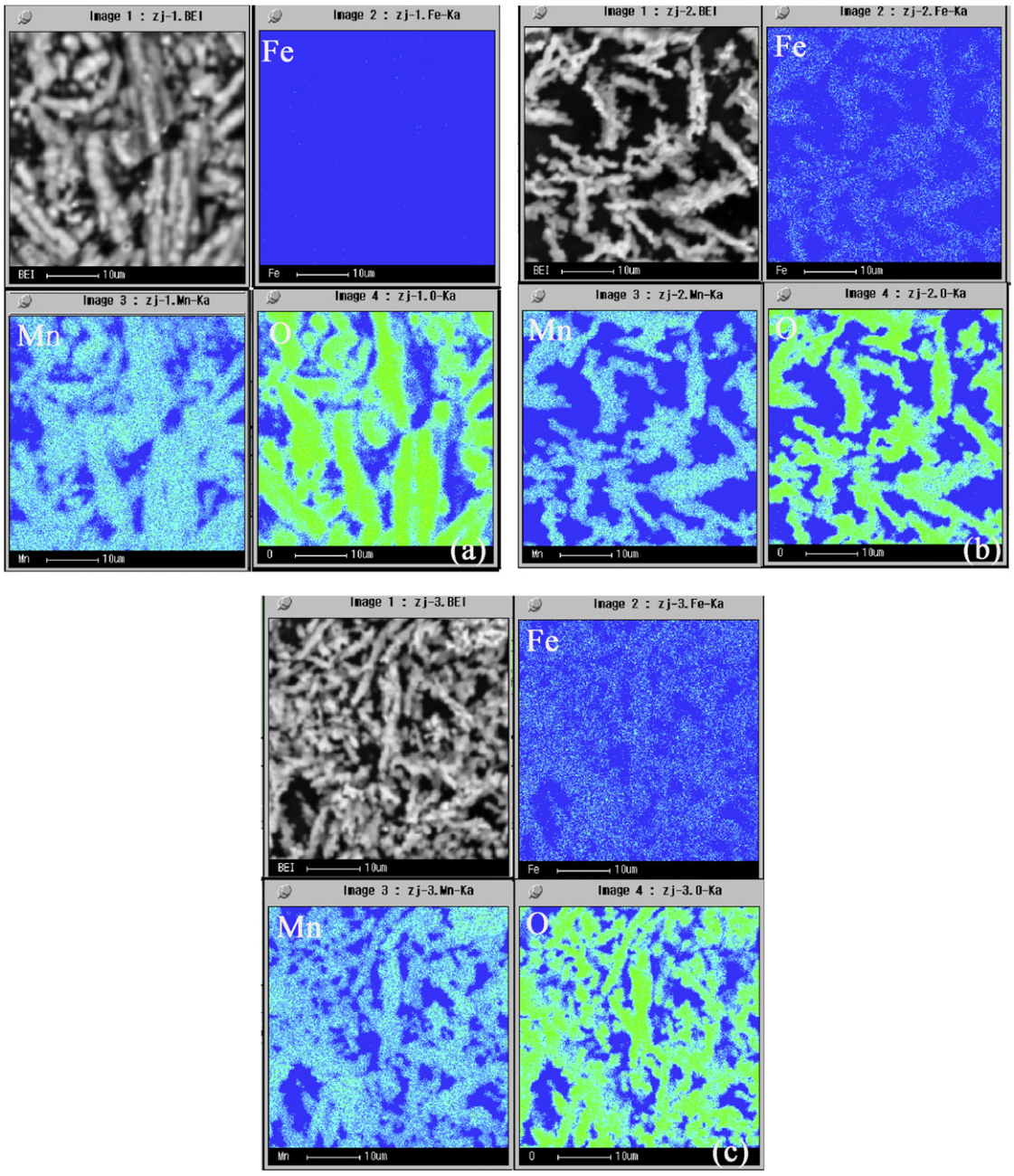

Fig. 2. Surface composition analysis images of the samples. (a) S1: without Fe; (b) S2: with 1/9 Fe/Mn; and (c) S3: with 1/4 Fe/Mn.

and the electrochemical properties of MnO_2 clearly improved with the doping of a metallic element into it. Our group synthesized MnO_2 powder in a high magnetic field [12,13] and found that the magnetic loss property of MnO_2 was enhanced, but this improvement remains insufficient. Therefore, doping a metallic element into MnO_2 and introducing an external field can be viewed as the important components of synthetic processes for materials with unique morphologies and properties. Few studies on the fabrication of Fe-doped MnO_2 under a high magnetic field for EM wave absorbents have been conducted.

In the present study, therefore, Fe-doped MnO_2 powder was synthesized under a high magnetic field. The morphology, form mechanism, novel electromagnetic properties, and EM wave-absorption properties of the Fe-doped MnO_2 products were investigated.

2. Experimental

2.1. Synthesis

All chemical reagents were commercially available and used as-received without further purification. Manganese sulfate ($MnSO_4 \cdot H_2O$), ammonium persulfate ($(NH_4)_2S_2O_8$), and ferrous sulfate ($FeSO_4 \cdot 7H_2O$) were purchased from the Dalian Shenlian Chemical Reagent, Co. (China).

In a typical synthesis process, 80 mL mixed solution of $MnSO_4 \cdot H_2O$ and $FeSO_4 \cdot 7H_2O$ with different proportions were prepared. The selected proportions of Fe/Mn were 0/10, 1/9, and 1/4. To obtain better experimental results, a comparative experiment was designed in which the same amounts of $MnSO_4 \cdot H_2O$ and $(NH_4)_2S_2O_8$ were used as the only reactants. Subsequently,

0.084 mol $(NH_4)_2S_2O_8$ was added into the mixture. Immediately, the color of the solution became orange because of the formation of Fe^{3+}. The solution was stirred adequately for 30 min at room temperature. The solution was transferred to a glass test tube and heated to boiling point, and maintained at this temperature for 1 h under a 10 T high magnetic field. The glass test tube was then allowed to cool to room temperature. The black products were filtered, washed several times with distilled water and absolute ethanol, and then dried under vacuum at 60 °C for 24 h. The samples were designated as S1, S2, and S3, corresponding to the proportions of Fe/Mn (0/10, 1/9, and 1/4, respectively).

2.2. Characterization

Phase identifications were performed by X-ray powder diffraction (SHIMADZU, XRD-6000, 40 kV/30 mA) with Cu$K\alpha$ radiation (λ=0.15406 nm) in the 2θ range of 10–100° with a step size of 0.04°, using the detector technique for measuring intensities. The microstructural features of MnO_2 were observed by scanning electron microscopy (SEM, JEOL JSM-5600LV) at an accelerating voltage of 20 kV. Transmission electron microscopic (TEM) images, high-resolution TEM (HRTEM) images, and selected area electron diffraction (SAED) patterns were generated using a TECNAI $G^2$20S-Twin TEM (accelerating voltage, 200 kV). Surface composition analysis was performed using an electron probe X-ray microanalyzer (EPMA-1600, acceleration voltage 15 kV).

The measurements of relative complex permittivity and permeability versus frequency were carried out by reflection/transmission technology using an Agilent 8722ES network analyzer. The as-obtained MnO_2 was dispersed in molten paraffin wax, and the uniform mixtures were molded into toroid-shaped samples of 7.00 mm in outer diameter and 3.00 mm in inner diameter. The specimens, consisting of 30 wt% MnO_2 powders, were measured within 2–18 GHz. The microwave absorption properties of the MnO_2/paraffin wax samples were calculated according to transmission line theory.

3. Results and discussion

3.1. Phase structure and surface composition analysis

As shown in Fig. 1, the XRD patterns of the three samples have large similarities with those of pure α-MnO_2 because no extra peaks appear during the second phase. All the diffraction peaks can be indexed to tetragonal (JCPDS card 44-0141) MnO_2. We deduce that because of the relatively small amount of Fe and the broad diffraction peaks, the peaks in the extra phase containing Fe are too weak, causing them to coincide with the broad peaks of the α-MnO_2 phase. Moreover, with increasing amounts of Fe, the intensity of the diffraction peaks weakens, indicating poor crystallinity.

Fig. 2 shows the images of the surface composition analysis of the Fe, Mn, and O samples. As shown in the figure, Fe is clearly successfully doped in the samples S2 and S3, even though the Fe content is minimal. Moreover, Fe is distributed uniformly in the sea urchin-like ball chain structures.

From the analysis above, because of the absence of the second phase, Fe possibly enters the MnO_2 structure and forms the solid solution. Furthermore, given that the atomic radius of Fe is close (slightly smaller) to that of Mn, the solid solution formed belongs to the substitution solid solution. Fig. 3, the schematic of the crystalline structure, shows that MnO_2 has rutile structure. A Mn atom is in the center and vertices of the tetragonal system structure. Hence, after Fe is substituted to Mn, a crystalline structure is a probable result (Fig. 3(b)). In addition, after Fe is substituted to Mn, contraction of the lattice occurs because of the smaller atomic radius of Fe, which corresponds to the calculated cell volume as shown in Table 1.

3.2. Morphology analysis

Figs. 4 and 5 show the SEM and TEM images of the samples with different Fe/Mn proportions. Although the existence of Fe does not influence the crystalline structure, the morphologies of the samples are clearly different. As shown in the figures, the sea urchin-like ball chain structures appear in all the samples. However, when MnO_2 is doped with Fe, the agglomeration of the sea urchin-like ball chains became serious, and the sea urchin-like ball becomes more compact. In doped samples S2 and S3, the sea urchin-like microspheres are hollow. With increasing Fe content, the size of the sea urchin-like ball markedly diminishes. Thus, the smaller size of the sea urchin-like ball easily causes palpable agglomeration. The smaller size of the doped sample may be attributed to the iron oxide on the surface of the MnO_2 microspheres preventing the MnO_2 particles from expanding further. The inset of the diffraction pattern images in Fig. 5 shows that the crystallization degree of Fe-doped samples S2 and S3 decreases compared with that of S1 (undoped). The HRTEM images provide more detailed structural information about the stick on the surface of the microspheres, showing the apparent lattice fringes of the crystal.

A possible mechanism for the formation of the hollow sea urchin-like ball chain shape can be described as follows: during the initial stage, some small and unstable particles with higher surface energies, are produced first (Fig. 6(a)). Subsequently, these

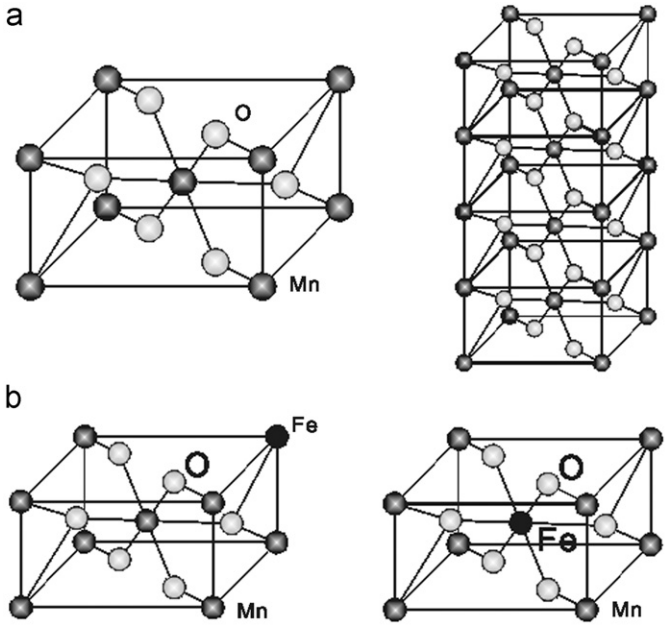

Fig. 3. Schematic of the crystalline structure of Fe-doped MnO_2 material.

Table 1
Calculated cell volume and c/a values of the three samples.

Sample	Proportions of Fe/Mn	Cell volume	c/a
S1	0/10	279.088	0.288
S2	1/9	278.806	0.289
S3	1/4	276.030	0.292

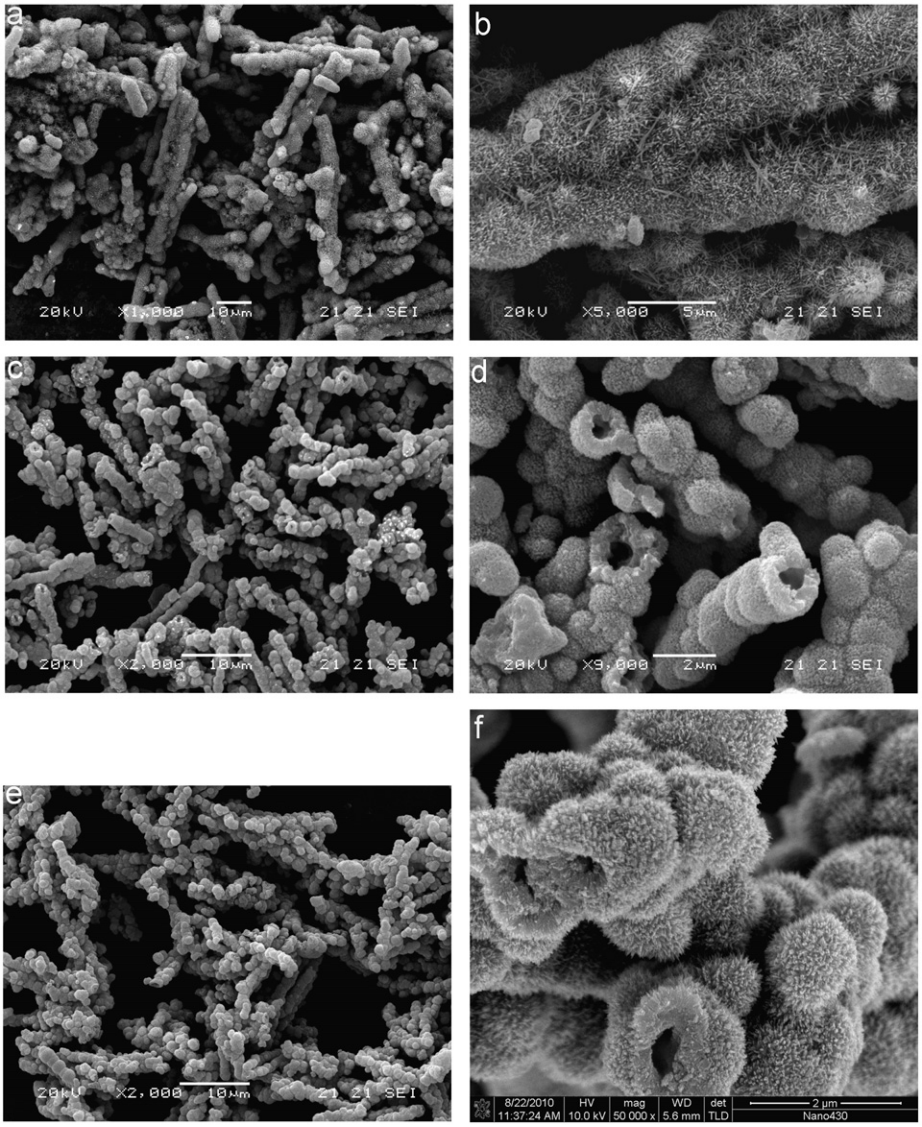

Fig. 4. SEM images of the samples with different Fe/Mn proportions. (a) and (b) S1: the sample without Fe; (c) and (d) S2: with 1/9 Fe/Mn; (e) and (f) S3: with 1/4 Fe/Mn.

small particles congregate to the relatively larger particles to decrease the energy of the entire system (Fig. 6(b) and (c)). As the reaction progresses, the reactants in the reaction system are depleted and the reaction system transforms into a thermodynamically stable state. Meanwhile, because of the difference between the interior and the exterior environments of the spherical agglomeration and the one-dimensional growth habit of MnO_2 crystals, the exterior particles gradually increase in size and form some acerose nanoparticles (Fig. 6(d)). The interior particles have higher surface energies than the exterior surface; thus, they tended to dissolve concomitant with an Ostwald ripening process [14]. Moreover, because of the addition of Fe, the ionic concentration of the reaction system and the chemical potential of the solution increased, thereby accelerating the pace of the entire process. With Fe^{3+}, the hollow structure is easily generated by the Ostwald process (Fig. 6(e)). The deduced formation mechanism of the hollow sea urchin-like ball is similar to that proposed by He et al. [15]. These microspheres, which array randomly in the absence of a high magnetic field, arrange themselves along a given direction under the external magnetic field. For any kind of crystal, differences in the arrangement and the density of the atomic structure result in differences in the magnetic susceptibilities of the same crystal at different crystallographic orientations. Small-sized microspheres arrayed along the direction of their maximum magnetic susceptibility (which is also along the magnetic field) are equivalent to small magnetic bodies. Consequently, they assemble to form the hollow sea urchin-like ball chain (Fig. 6(f)).

3.3. Electromagnetic properties

Complex permittivity, permeability, and their corresponding loss tangents represent the dielectric and magnetic properties of an absorbing material. The real parts (ε' and μ') of complex permittivity and permeability correspond to the storage capabilities of electric and magnetic energy. The imaginary parts (ε'' and μ'') represent the loss of electric and magnetic energy [16]. The loss tangent ($\tan\delta$) represents the loss properties of the incidence EM wave in the microwave absorber.

Fig. 7(a) and (b) shows the relative complex permittivity and permeability of the samples in the frequency range of 2–18 GHz. In Fig. 7(a), with increasing Fe content, both the ε' and ε'' values decline throughout the entire frequency range. Moreover, the ε' and ε'' values of the sample S1 exhibit relatively obvious

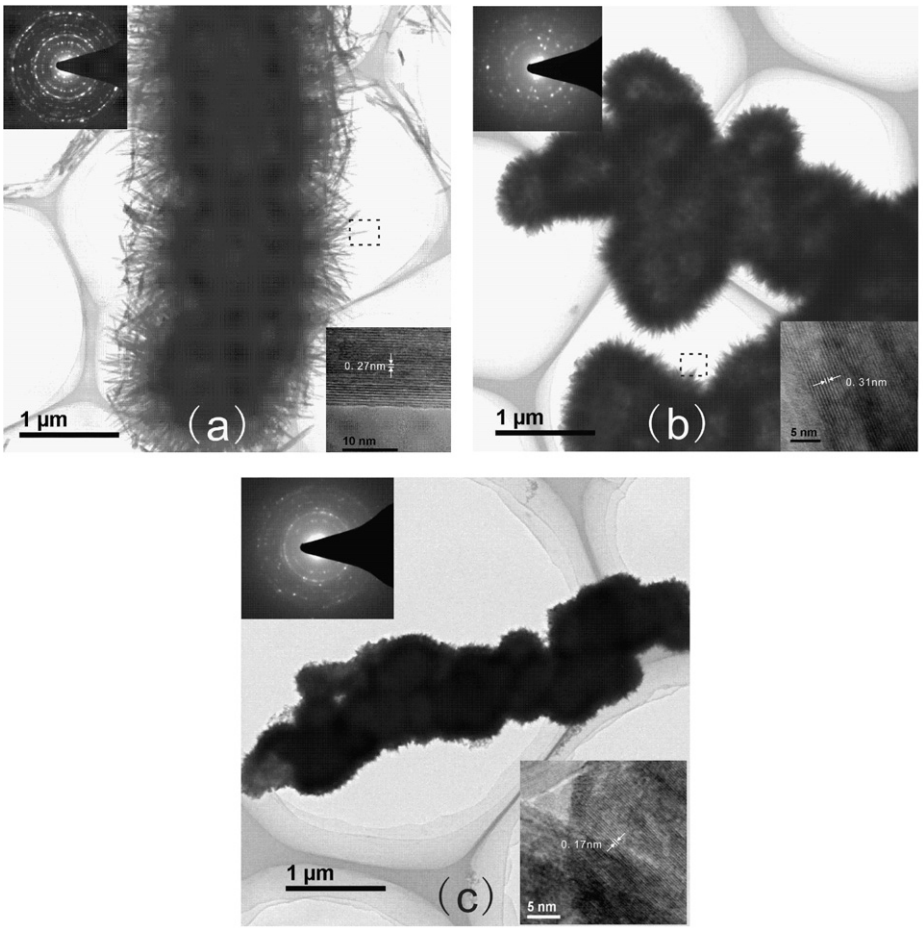

Fig. 5. TEM images with diffraction patterns (inset) and HRTEM images of the samples with different Fe/Mn proportions. HRTEM images were obtained from the rectangular regions. (a) S1: without Fe; (b) S2: with 1/9 Fe/Mn; and (c) S3: with 1/4 Fe/Mn.

reduction as frequency increases. The ε' and ε'' values of S2 and S3 have less variation with increasing frequency. Between 14 and 18 GHz, the ε'' values of S2 and S3 increase slightly as frequency increases. The ε' scopes of S1, S2, and S3 are 8.214–4.657, 4.042–3.424, and 3.320–3.468, respectively. Moreover, the ε'' scopes of the samples are 2.802–2.035, 0.698–1.064, and 0.239–0.959, respectively. Fig. 7(b) shows that with increasing Fe content, both the μ' and μ'' values increase in the entire frequency range. Furthermore, the μ' values of S1 and S2 have less variation (0.960 and 1.085, respectively). In S3, the μ' value exhibits a slight fluctuation in the entire frequency range (1.19–1.269). The μ'' value of S1 is constant in the entire frequency range (0.020). On the other hand, in S2 and S3, the μ'' values show a slight increase, and the scopes are 0.034–0.136 and 0.057–0.28, respectively.

Fig. 8(a) and (b) shows the frequency dependence of the electric loss tangent and magnetic loss tangent of the samples. With increasing Fe content, the tan ε values decline within the entire frequency range, corresponding to the data shown in Fig. 7(a). Furthermore, the tan ε value of S1 shows a slight increase with increasing frequency (0.341–0.43). In S2 and S3, the tan ε values also exhibit a slight decrease between 2 and 12 GHz, and then markedly increase between 12 and 18 GHz. The tan ε scopes of S2 and S3 are 0.173–0.311 and 0.072–0.277, respectively. As shown in Fig. 8(b), with increasing Fe content, the tan μ values increase in the entire frequency range, corresponding to the data depicted in Fig. 7(b). Moreover, the tan μ value of S1 has less variation, and the scope is 0.018–0.034. By contrast, in S2 and S3, the tan μ values markedly increase with scopes are 0.031–0.121 and 0.045–0.223, respectively.

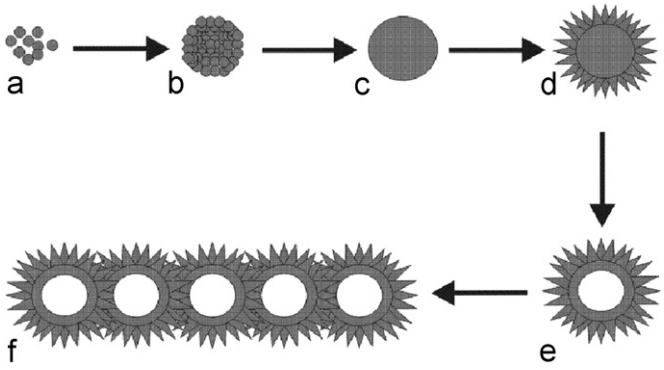

Fig. 6. Schematic representation of the formation of the hollow sea urchin-like microsphere chain shape.

Based on the data above, doping MnO_2 with Fe clearly exerts considerable influence on the EM properties of the prepared MnO_2 powder. By doping MnO_2 with Fe, the relative complex permittivity of MnO_2 and its corresponding loss tangent clearly decreases, but the relative complex permeability of MnO_2 and its corresponding loss tangent substantially increase. We deduce that after doping MnO_2 with Fe, the lattice distortion caused by the generated solid solution clearly decreases the relative complex permittivity of MnO_2 and its corresponding loss tangent.

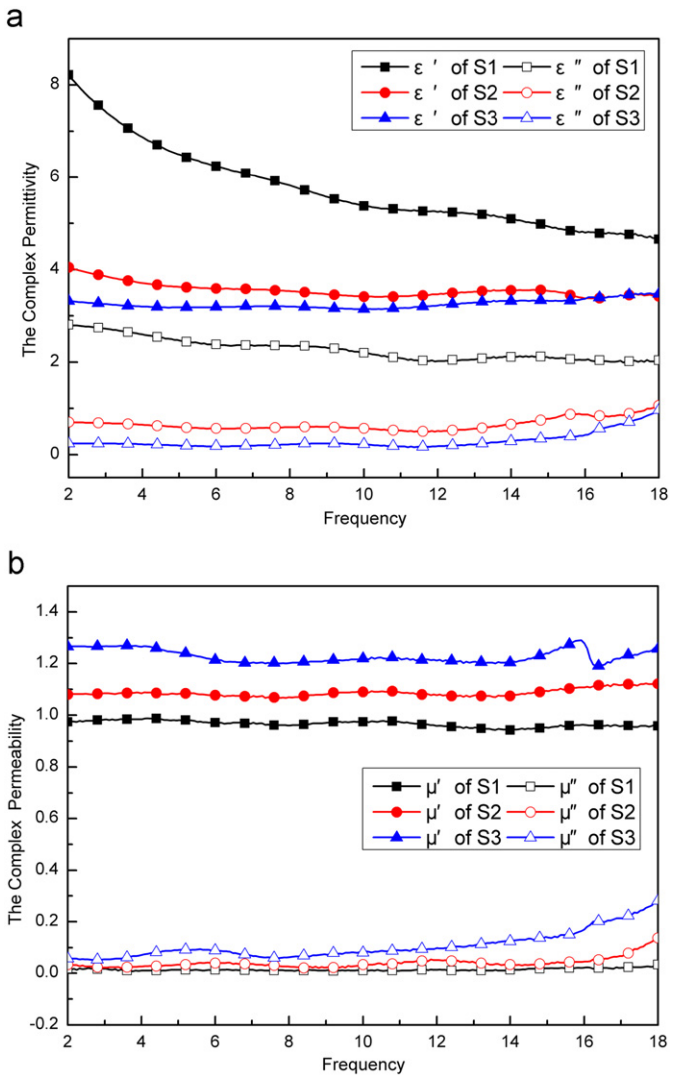

Fig. 7. Relative complex permittivity and permeability of the samples within 2–18 GHz. (a) Complex permittivity and (b) complex permeability. S1: without Fe; S2: with 1/9 Fe/Mn; S3: with 1/4 Fe/Mn.

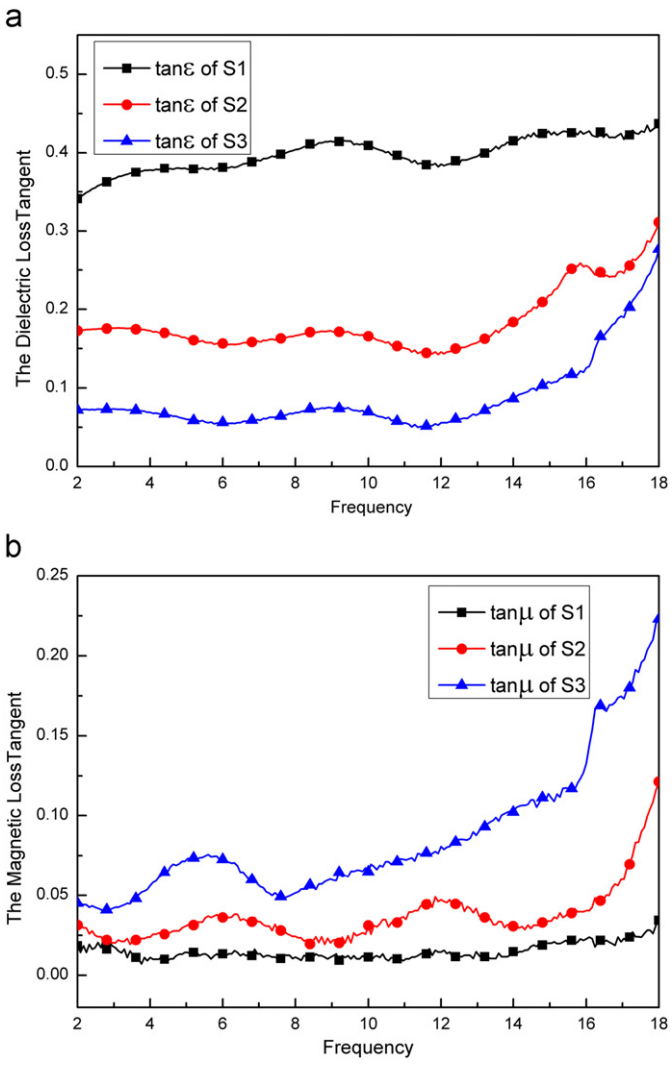

Fig. 8. Electric loss tangent and magnetic loss tangent of the samples within 2–18 GHz. (a) Electric loss tangent value and (b) magnetic loss tangent value. S1: without Fe; S2: with 1/9 Fe/Mn; S3: with 1/4 Fe/Mn.

According to Zhang et al. [17], inherent relationships between the dielectric properties and lattice distortions in PZT ferroelectric tetragonal phase region exist, and they found that smaller c/a values increase permittivity. Similarly, in the present study, with increasing Fe content, the c/a values of the Fe-doped MnO_2 samples increase slightly, as shown in Table 1. The larger c/a values of the Fe-doped samples probably result in lower permittivity. In addition, the solid solution containing Fe has relatively good magnetic properties. Hence, the relative complex permeability of MnO_2 and its corresponding loss tangent substantially increases after doping with Fe.

3.4. Electromagnetic wave absorption properties

From the dependence of the microwave absorption properties on permittivity and the permeability, the reflection losses [R(dB)] were calculated according to transmission line theory [18]. The normalized input impedance Z_{in} of a microwave absorber is given by

$$Z_{in} = \sqrt{\frac{\mu_r}{\varepsilon_r}} \tanh\left[j\frac{2\pi}{c}\sqrt{\mu_r\varepsilon_r} f d\right] \quad (1)$$

where μ_r and ε_r are the relative permeability and permittivity of the composite medium, respectively, c is the velocity of EM waves in free space, f denotes the frequency of the microwave, and d is the thickness of the absorber. The reflection loss is related to Z_{in} as

$$\text{Reflection loss(dB)} = 20\log\left|\frac{Z_{in}-Z_0}{Z_{in}+Z_0}\right| \quad (2)$$

where $Z_0 = \sqrt{\mu_0/\varepsilon_0}$ is the characteristic impedance of free space.

Thus, the reflection loss of an absorber is a function of six characteristic parameters ε',ε'',μ',μ'', f, and d. The values of the parameters ε',ε'',μ',μ'' have been previously obtained (Fig. 7), and the thickness d is assumed to be 0.5 mm. The reflection losses of the Fe-doped MnO_2/paraffin wax samples were calculated from a computer simulation using Eq. (2). The reflection losses as a function of the frequency for the samples with different Fe-doped MnO_2 proportions are obtained and shown in Fig. 9.

Fig. 9 shows the calculated reflection loss of the 30 wt% MnO_2/paraffin wax composites. The as-prepared Fe-doped MnO_2 sample has good microwave absorption capability compared with pure MnO_2 materials. From the shape of the curve, with increasing Fe content, the absorption curves clearly become more precipitated

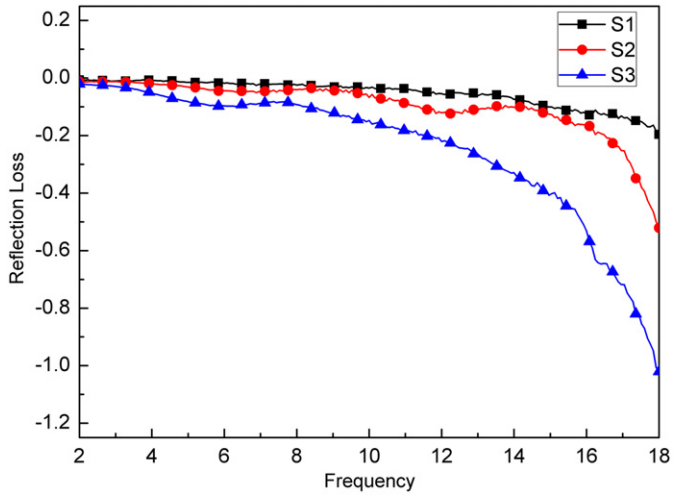

Fig. 9. Calculated reflection loss of the 30 wt% MnO_2/paraffin wax composites with a 0.5 mm thick within 2–18 GHz. S1: without Fe; S2: with 1/9 Fe/Mn; S3: with 1/4 Fe/Mn.

and show more outstanding microwave absorption properties. Within 2–18 GHz, S3 exhibits a maximum reflection loss of −1.02 dB at 18 GHz.

The good microwave absorption capability of the sample can be attributed to the small permittivity of the Fe-doped MnO_2. The input impedance Z_{in} of the Fe-doped MnO_2 is close to the impedance of the free space Z_0. Hence, the EM wave can be adequately transmitted into the interior of the samples, which is a necessary condition for the loss of incidence EM wave. Furthermore, based on the results of phase structure and morphology analysis, Fe-doped MnO_2 forms a substitution solid solution in which lattice distortion occurs, and its morphology is a hollow urchin-like ball chain. Under the alternating EM fields, the interfacial and space-charge polarization are easily formed on the interface and the interior of the Fe-doped MnO_2 samples. Therefore, the reflection loss is attributed to the polarization relaxation loss of the Fe-doped MnO_2 particles. In addition, based on the analysis of the EM properties, the improved permeability plays an important role in improving the magnetic loss properties of MnO_2. Thus, the microwave-absorbing property of the Fe-doped MnO_2 samples is better than that of the pure MnO_2. The new Fe-doped MnO_2 materials is a potentially good EM absorbent.

4. Conclusions

Fe-doped MnO_2 with a hollow sea urchin-like ball chain shape was successfully synthesized in a high magnetic field of 10 T. Its major components are α-MnO_2 and its lattice structure belong to a substitution solid solution. By doping MnO_2 with Fe, the relative complex permittivity of MnO_2 and its corresponding loss tangent properties clearly decreased, but the relative complex permeability of MnO_2 and its corresponding loss tangent properties markedly increased. Moreover, the theoretically calculated values of reflection loss show that with increasing Fe content, the as-prepared Fe-doped MnO_2 materials exhibits good microwave absorption capability compared with pure MnO_2 materials.

Acknowledgments

The authors acknowledge the support from the National Natural Science Foundation of China (No. 51007005), The Research Fund for the Doctoral Program of Higher Education of China (20090041120038), The Aero Science Foundation of China (20095463008), and The Fundamental Research Funds for the Central Universities and the Growth Foundation for the Youth Teachers of the Dalian University of Technology.

Appendix A. Supporting information

Supplementary data associated with this article can be found in the online version at doi:10.1016/j.jssc.2011.03.007.

References

[1] D. Yan, S. Cheng, R.F. Zhuo, J.T. Chen, J.J. Feng, H.T. Feng, H.J. Li, Z.G. Wu, J. Wang, P.X. Yan, Nanotechnology 20 (10) (2009) 105706.
[2] H.M. Huang, S. Mao, H. Feick, H. Yan, Y. Wu, H. King, E. Weber, R. Russo, P. Yang, Science 292 (2001) 1897–1899.
[3] L. Jin, C.H. Chen, V.M.B. Crisostomo, L.P. Xu, Y.C. Son, S.L. Suib., Applied Catalysis A: General 355 (2009) 169–175.
[4] J. Lee, J.M. Lee, S. Yoon, S.O. Kim, J.S. Sohn, K.I. Rhee, H.J. Sohn, Journal of Power Sources 183 (2008) 325–329.
[5] Y.P. Duan, H. Ma, J. Zhang, X.G. Li, S.H. Liu, Chinese Journal of Inorganic Chemistry 25 (9) (2009) 1635–1641.
[6] Y.P. Duan, H. Ma, X.G. Li, S.H. Liu, Z.J. Ji., Physica B: Condensed Matter 405 (2010) 1826–1831.
[7] G. Wang, B. Tang, L. Zhuo, J. Ge, M. Xue, European Journal of Inorganic Chemistry 2006 (11) (2006) 2313–2317.
[8] J. Ge, L. Zhuo, F. Yang, B. Tang, L. Wu, C. Tung.Journal of Physical Chemistry B 110 (36) (2006) 17854–17859.
[9] R. Patrice, L. Dupont, L. Aldon, J.C. Jumas, E. Wang, J.M. Tarascon, Chemistry of Materials 16 (2004) 2772–2782.
[10] M. Liu, G.J. Zhang, Z.R. Shen, P.C. Sun, D.T. Ding, T.H. Chen, Solid State Sciences 11 (2009) 118–128.
[11] X.L. Li, W.J. Li, X.Y. Chen, C.W. Shi, Journal of Crystal Growth 297 (2006) 387–389.
[12] J. Zhang, Y.P. Duan, S.Q. Li, X.G. Li, S.H. Liu., Journal of Solid State Chemistry 183 (2010) 1490–1495.
[13] J. Zhang, Y.P. Duan, H. Jing, X.G. Li, S.H. Liu, S.Q. Li., Journal of Crystal Growth 312 (2010) 2788–2794.
[14] H.C. Zeng., Current Nanoscience 3 (2007) 177–181.
[15] X.X. He, M.Y. Yang, P. Ni, Y. Li, Z.H. Liu, Colloids and Surfaces A: Physicochemical and Engineering Aspects 363 (2010) 64–70.
[16] N. Chen, G.H. Mu, X.F. Pan, K.K. Gan, M.Y. Gu, Materials Science and Engineering 139 (2007) 256–260.
[17] D.M. Zhang, W.S. Yan, Z.C. Zhong, F.X. Yang, K.Y. Zheng, Z.H. Li, Acta Physica Sinica 53 (05) 1316-05.
[18] H.T. Guan, Y.B. Zhao, S.H. Liu, S.P. Lv, European Physical Journal Applied Physics 26 (2006) 235–239.